PRECISE ATTITUDE ESTIMATION OF AN ADR TARGET OBJECT BY COMPREHENSIVE COMPARISONS OF OBSERVED AND CG-BASED LIGHT CURVES

Hiroshi Oda, Masato Hayashi, Toshifumi Yanagisawa, Hirohisa Kurosaki, Kohki Kamiya, Manuel Cegarra Polo, Ryusuke Harada, and Satomi Kawamoto

Japan Aerospace Exploration Agency, 7-44-1 Jindaiji-Higashi-machi, Chofu, Tokyo 182-8522, Japan, Email: {oda.hiroshi, hayashi.masato, yanagisawa.toshifumi, kurosaki.hirohisa, kamiya.kohki, cegarrapolo.manue, harada.ryuusuke, kawamoto.satomi}@jaxa.jp

ABSTRACT

Active debris removal (ADR) is crucial for suppressin the growth of space debris and stabilizing the space environment in LEO regime. In an ADR mission, the state of target object should be precisely investigated in advance. Photometric light curves from ground-based telescopes include valuable information, such as the object's attitude, size, shape, and surface properties. Light curve analysis can be an effective method for estimating their attitude for objects with known size, shape, and surface properties. This study focuses on the attitude estimation of the H2-A rocket upper stage, a target object for ADR, using comparisons between observed and simulated light curves. In our light curve simulation using the 3D CG model, diffuse reflection (using the Lambertian diffuse reflection model) and specular reflection (using the Blinn-Phong reflection model) are considered. As a result of the comprehensive comparisons, we found that the light curves suggest that the target object is almost stationary with the attitude expected from gravity-gradient stabilization. However, the estimated attitude is not perfectly stationary. There is a variation within a range of about 1-2 degrees between each observed light curve. This result suggests the possibility of slight oscillations around the attitude expected from the gravity-gradient stabilization.

Keywords: Light curve; Photometric observation; Attitude estimation; LEO; ADR.

1. INTRODUCTION

The space debris population has been growing due to the increasing number of space activities. Active debris removal (ADR) is essential to suppress the growth of the space debris population and stabilize the space environment, particularly in the LEO regime.

In an ADR mission, the state of the target object should be precisely investigated in advance. Furthermore, such information about the state of the target object can be valuable in case of contingencies. Photometric light curves obtained from ground-based optical telescopes contain information about the state of target objects, such as their attitude, size, shape, and surface properties. Light curve inversion has primarily been used to estimate the shapes and rotational characteristics of natural bodies such as asteroids, where the shape is generally assumed to be smooth and approximately convex. In contrast, the shape and surface reflectivity of space debris are usually more complex. However, for objects with known size, shape, and surface reflectivity, light curve analysis can be an effective method for estimating their attitude.

In general, the light curves of tumbling objects exhibit periodic variations over time. Several studies have been conducted on determining the rotation period, rotation axis, and precession motion of tumbling objects from light curves. (e.g, [3], [1], [2]). On the other hand, the light curves of nearly stationary or slowly tumbling objects primarily vary depending on their attitude and phase angle (the angle between the Sun, object, and observer). Tumbling objects with high rotation speeds are beyond the scope of this study, as we focus on candidate objects for the specific ADR mission mentioned below. In [4], an optical simulator using a scale model of the second stage of the Japanese H-2A rocket (H-2A R/B) is employed to mimic the observed light curves in the laboratory. They found that in some cases, the simulated light curve, assuming the attitude expected from gravity-gradient stabilization, is roughly consistent with the observed light curve, and that the peak position in the light curve is important for estimating the attitude. However, it was not practical to conduct a comprehensive comparison using this method, as experiments with the optical simulator are time-consuming. The primary objective of this work is to precisely estimate the attitude of nearly stationary or slowly tumbling objects through comprehensive comparisons using CG-based simulations.

In this paper, we focus on the H-2A R/B (International Designator 2009-002J / SSC 33500), which is the target object of the Commercial Removal of Debris Demonstration (CRD2) program conducted by the Japan Aerospace

Proc. 9th European Conference on Space Debris, Bonn, Germany, 1–4 April 2025, published by the ESA Space Debris Office
Editors: S. Lemmens, T. Flohrer & F. Schmitz, (http://conference.sdo.esoc.esa.int, April 2025)

Exploration Agency (JAXA). Information on the dimensions of this object and the surface materials of some parts is available to the authors, which is useful for constructing a 3D CG model of the object. In addition, images of the target object have been directly captured from a distance of 50 meters by the demonstration satellite ADRAS-J (Active Debris Removal by Astroscale-Japan; the CRD2 Phase I demonstration satellite developed, owned, and operated by Astroscale Japan Inc. https://astroscale.com/) during the "Fly-around observation service". This object is not only a target of the ADR mission but also a rare case where direct images are available.

We conducted optical observations to obtain photometric light curves of the target object using the 0.35-meter aperture telescope with a CMOS sensor at JAXA Chofu Aerospace center in Tokyo, Japan, and the 0.6-meter aperture telescope with a CMOS sensor at Mt. Nyukasa observatory in Nagano, Japan. The basic orbital information of the object (as of July 28, 2024) is as follows: the semi-major axis is 6962 km, with an apogee of 613 km, a perigee of 555 km, and an inclination angle of 98 °. The typical duration of a visible pass from these sites is several hundred seconds.

We constructed a 3D CG model of the target object and simulated light curves for given (parameterized) attitudes and surface properties. The orbit, and therefore the phase angle, was calculated using two-line-element (TLE). We evaluate the residuals between the photometric light curve and the simulated light curves with various parameters. The case with the lower evaluation value is considered the more plausible solution. In this paper, we present the results of comprehensive comparisons. As a result, we were able to estimate the attitude of the target object within a few degrees.

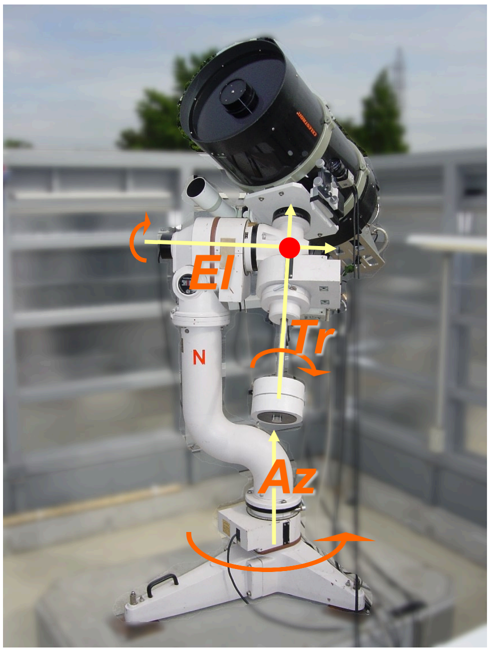

Figure 1. The 0.35-meter aperture telescope mounted on the tri-axial alt-azimuth mount with a CMOS sensor at JAXA Chofu Aerospace center in Tokyo, Japan

2. OPTICAL OBSERVATION

The light curves were acquired using the 0.35-meter aperture telescope mounted on the tri-axial alt-azimuth mount with a CMOS sensor at the JAXA Chofu Aerospace Center in Tokyo, Japan (Fig. 1), and the 0.6-meter aperture telescope mounted on the (common two-axis) alt-azimuth mount with a CMOS sensor at Mt. Nyukasa observatory in Nagano, Japan (Fig. 2). The distance between the two sites is approximately 130 km. The typical observation duration for each light curve is several hundred seconds, varying depending on the duration of the target object's visible pass. The exposure time is basically set in the range of 50 ms to 200 ms, depending on the brightness of the target object and the sky conditions.

Figure 2. The 0.6-meter aperture telescope with a CMOS sensor at Mt. Nyukasa observatory in Nagano, Japan.

Fig. 3 shows a sample light curve of 33500 acquired using Chofu and Nyukasa telescopes. In the early stages of this study, a comprehensive parameter survey revealed that the light curves suggest the target object is nearly stationary, with the PAF (Payload Attach Fitting) pointing in the nadir direction, as expected from gravity-gradient

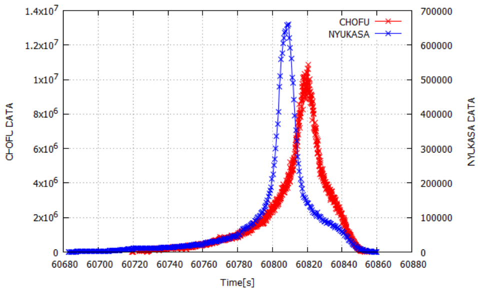

Figure 3. The observed light curve of 33500 acquired using Chofu telescope(red) and Nyukasa telescope(blue) on 2023.06.05

stabilization (See also [4]). In addition, the peak seen in Fig. 3 is important to precisely estimate the attitude of this target object. For this reason, we designed our observation plans to capture such peaks as frequently as possible. Assuming that the target object remains nearly stationary with the PAF pointing in the nadir direction, we predicted light curves up to one week in advance using TLE orbit and the 3D CG model. We then identified the nights when the specular reflection component from PSS would appear in the light curve. In this paper, we focus on the analysis of light curves that exhibit such peaks.

3. ANALYSIS METHOD

3.1. Light curve simulation model

In our CG-based simulations, we employ the extended Blinn-Phong reflection model. The intensity is given by

$$I = I_s + I_d \tag{1}$$

$$I_s = l \times [k_{s1} \cdot \cos^{m1}(\alpha) + k_{s2} \cdot \cos^{m2}(\alpha)] \tag{2}$$

$$I_d = l \times [k_d \cdot \cos(\theta_{in})] \tag{3}$$

where I_s is the specular reflection component, I_d is the diffuse reflection component(Lambertian diffuse reflection model), l is the intensity of the incident light, $\boldsymbol{V}$ is the observation unit vector, $\boldsymbol{L}$ is the illumination unit vector, $\boldsymbol{R}$ is the reflection unit vector, $\boldsymbol{H}$ is the angular bisector of $\boldsymbol{L}$ and $\boldsymbol{V}$ (the phase angle bisector vector), $\boldsymbol{N}$ is the surface normal unit vector, α is the angle between $\boldsymbol{H}$ and $\boldsymbol{N}$, θ_{in} is the angle between $\boldsymbol{L}$ and $\boldsymbol{N}$, k_d is the coefficient of diffuse reflection, k_{s1} and k_{s2} are the coefficients of specular reflection, m_1 and m_2 are the shininess of specular reflection (Fig. 4). Here, we introduce two reflection components characterised by the parameters [k_{s1}, m_1] and [k_{s2}, m_2] to improve the reflection properties at angles away from the line-of-sight vector, based on measurements of the Bidirectional Reflectance Distribution Function (BRDF) of the material composing the rocket body.

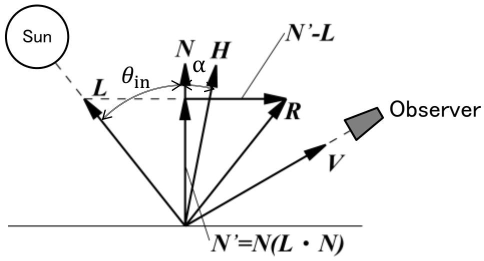

Figure 4. Reflection geometory

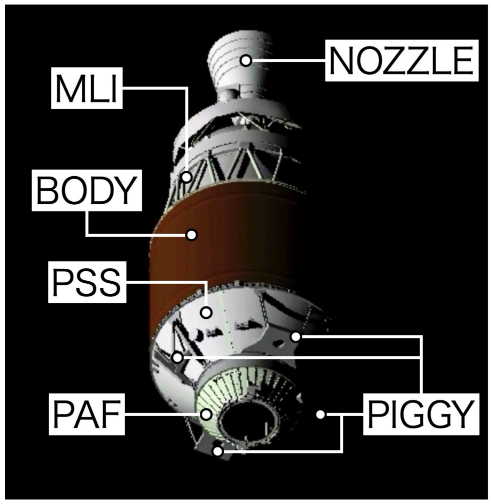

Figure 5. Overview of 3D CG model of the target object. The main segments of the 3D CG model are BODY, PAF, PSS, PIGGY (consisting of four parts), NOSSLE, and MLI. Note that the geometory of PIGGY has 180-degree rotational symmetry except for slight differences.

The main segments of the 3D CG model are BODY, PAF (Payload Attach Fitting), PSS (Payload Support Structure), PIGGY (consisting of four parts), NOSSLE, and MLI (Multi Layer Insulation) (Fig. 5).

We consider the diffuse reflection (Lambertian diffuse reflection model) and the specular reflection (extended Blinn-Phong reflection model). The reflective characteristics of each segment can be independently adjusted by modifying parameters such as the diffuse reflection coefficient, specular reflection coefficient, and shininess. We set these parameters with reference to the reflectance peaks in the BRDF measurements of the material used in each part.

The position of the target object during the observation period is calculated using the TLE orbit. Here, we introduce the angle [R_1, R_2, R_3]. R_1 and R_2 are the in-track and cross-track angles of the target object, respectively. R_3 specifies the angle around the cylinder axis of the target body (See Fig. 6). When [R_1, R_2] = [180°, 0°], the PAF-axis is pointing in the nadir direction.

For given attitude of the target object, the total intensity is computed by integrating the intensity from all surfaces

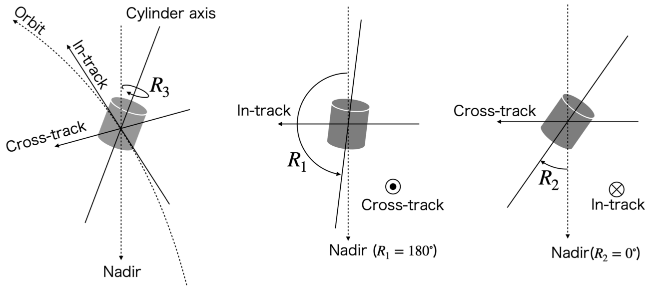

Figure 6. Schematic picture describing the in-track angle R_1, the cross-track angle R_2, and R_3.

(approximately 150,000 in total) of the 3D CG model. Fig. 7 shows a sample of the simulated light curve of 33500 for a given attitude and the CG image at the peak.

3.2. Evaluation method

According to the procedure in subsection 3.1, we compute light curves for a wide range of attutude. We evaluate the similarity between the observed light curve and the simulated light curves. In evaluating procedure, the light curves are normalised so that the time integral during the observation period is 100 (see Fig. 8). The sampling time is set to 1.0 s. We introduce the residual sum of absolute values (RSA) of the difference between the normalised observed light curve and the normalised simulated light curve as the evaluation value:

$$RSA = \sum_i |f(t_i) - g(t_i)| \tag{4}$$

where $f(t_i)$ and $g(t_i)$ are the values of the normalized observed and simulated light curves at the sampling time t_i, respectively. We aim to minimize the RSA by adjusting the attitudes. The case with the lower RSA is considered the more plausible solution.

4. COMPARISON OF THE OBSERVED AND SIMULATED LIGHT CURVES

4.1. Example of simultaneous light curves from two observation sites

On 2023.06.05, we acquired the light curves of 33500 using both the Chofu telescope and the Nyukasa telescope simultaneously. In this subsection, we present the analysis results of these light curves. We employ a coarse-to-fine search approach to reduce computational cost. As a first step, we evaluate the RSA in increments of $[\Delta R_1, \Delta R_2, \Delta R_3] = [5°, 5°, 30°]$ for all possible attitudes. Table 1 shows the top 5 ”Total” RSA values (the sum of the RSA values of ”Chofu” and ”Nyukasa”) for the light curves acquired using the Chofu telescope and the Nyukasa telescope on 2023.06.05.

Table 1. Top 5 RSA values in the first step (in increments of $[\Delta R_1, \Delta R_2, \Delta R_3] = [5°, 5°, 30°]$ for all possible attitudes.) ”Total” is the sum of the RSA values of ”Chofu” and ”Nyukasa”

Rank	Total	Chofu	Nyukasa	R_1	R_2	R_3
1	55.382	22.661	32.721	180	0	30
2	60.374	26.495	33.879	180	0	-30
3	67.819	31.340	36.479	180	0	60
4	69.543	23.011	46.532	180	0	-60
5	70.973	25.744	45.230	180	0	90

The upper panel of Fig. 9 shows the observed light curves using the Chofu telescope and the Nyukasa telescope and simulated light curves in tha case of the lowest RSA value ($[R_1, R_2, R_3] = [180°, 0°, 30°]$). The bottom panel shows each reflection component of the simulated light curves. The cases with $[R_1, R_2] = [180°, 0°]$ dominate the ranking. The simulated light curves are roughly fitted to the observed light curve and are dominated by the specular components of PSS and PAF. However, there is a discrepancy in the peak value and the shape after the peak, particularly in the Nyukasa light curve (dashed and dotted circle in Fig. 9).

We narrow down the search range based on the results of the first step. As a second step, we evaluate the residuals in increments of $[\Delta R_1, \Delta R_2, \Delta R_3] = [0.5°, 0.5°, 5°]$ within the range $[175° < R_1 < 185°, -5° < R_2 < 5°, -30° < R_3 < 30°]$. In the light curve fitting, the sensitivity to R_1 and R_2 is very high because the specular components from PSS and PAF are dominant. Therefore, we make the resolution of the in-track (R_1) and cross-track (R_2) angles very fine in this step. Table 4 shows the top 5 RSA values in the second step. Fig. 10 shows the light curves in the case of the lowest RSA value in the second step ($[R_1, R_2, R_3] = [179.0°, 2.5°, 10°]$) and the RSA value map on the R_1-R_2 plane for $R_3 = 10.0°$. We found that the discrepancy in the peak value becomes smaller, and the shape after the peak is dominated by the specular component from PIGGY.

As a third step, we evaluate the residuals in increments

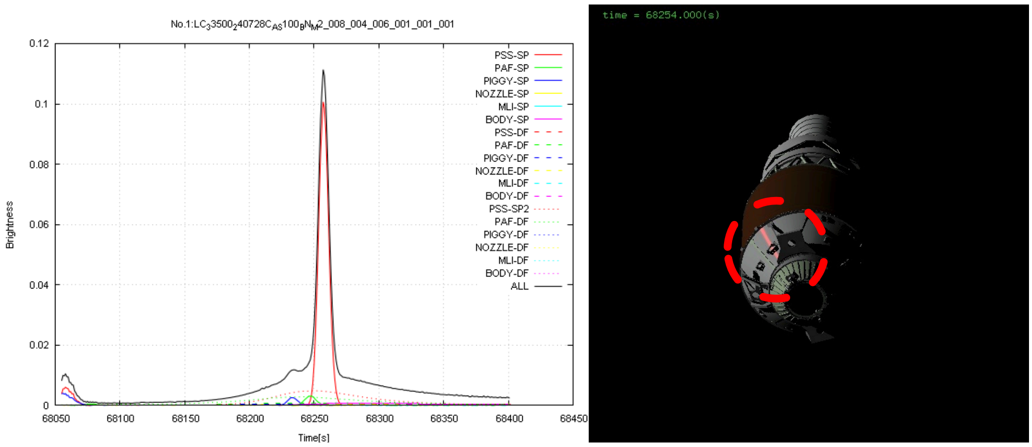

Figure 7. Left: Sample of the simulated light curve of 33500. Right: CG image at the peak. The dashed red circle represents the reflection area contributing the peak

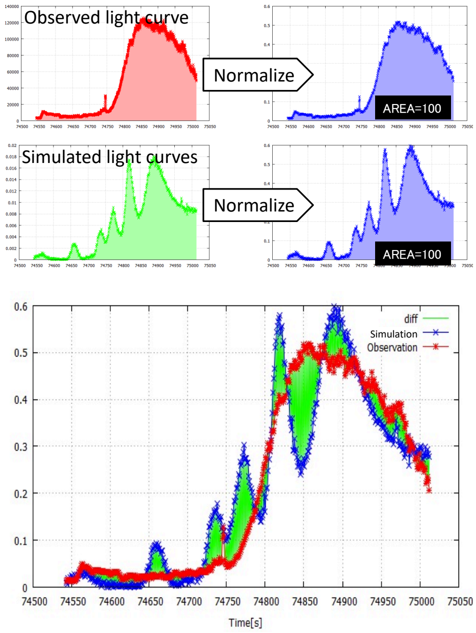

Figure 8. Top: Sample of normalisation of observed and simulated light curves. Bottom: Sample of difference between normalised light curves.

Table 2. Top 5 RSA values in the second step (in increments of $[\Delta R_1, \Delta R_2, \Delta R_3] = [0.5°, 0.5°, 5°]$ *within the range* $[175° < R_1 < 185°, -5° < R_2 < 5°, -30° < R_3 < 30°]$*).*

Rank	Total	Chofu	Nyukasa	R_1	R_2	R_3
1	32.962	15.469	17.493	179.0	2.5	10
2	33.773	15.481	18.292	179.0	3.0	10
3	35.645	15.779	19.866	180.5	-2.0	5
4	37.461	15.163	22.298	180.5	-2.5	5
5	37.628	21.804	15.824	178.5	4.0	10

Table 3. Top 5 RSA values in the third step (in increments of $[\Delta R_1, \Delta R_2, \Delta R_3] = [1.0°, 1.0°, 1.0°]$ *within the range* $[178° < R_1 < 182°, -2° < R_2 < 2°, -150° < R_3 < 210°]$*).*

Rank	Total	Chofu	Nyukasa	R_1	R_2	R_3
1	34.025	14.575	19.450	180	-1	6
2	34.064	14.276	19.789	180	0	187
3	35.337	15.770	19.567	180	-1	186
4	35.548	17.588	17.960	179	2	9
5	36.367	15.854	20.512	180	-1	7

of $[R_1, R_2, R_3] = [1.0°, 1.0°, 1.0°]$ within the range $[178° < R_1 < 182°, -2° < R_2 < 2°, -150° < R_3 < 210°]$. We narrow down the search range for the in-track (R_1) and cross-track (R_2) angles based on the result of the second step. In this step, we make the resolution of R_3 very fine. Table 3 shows the top 5 RSA values in the third step. We note that the geometory of PIGGY, consisting of four parts, (and therefore R_3) has 180-degree rotational symmetry except for slight differences.

As a fourth (final) step, we evaluate the residuals in increments of $[\Delta R_1, \Delta R_2, \Delta R_3] = [0.2°, 0.2°, 0.5°]$ within the range $[178° < R_1 < 182°, -5° < R_2 < 5°, 5° < R_3 < 10°]$. Fig. 11 shows the light curves for the case with the lowest RSA value in the fourth step ($[R_1, R_2, R_3] = [179.0°, 2.5°, 10°]$) and the RSA map on the R_1-R_2 plane for $R_3 = 9.0°$.

We also conducted comprehensive investigations to verify whether there are any more plausible solutions. Fig. 12 shows the RSA value map on the R_1-R_2 plane for $R_3 = 9.0°$, in increments of $[\Delta R_1, \Delta R_2] = [1°, 1°]$ within the range of $[-90° < R_1 < 270°, -90° < R_2 < 90°]$. We found that there are no other plausible solutions.

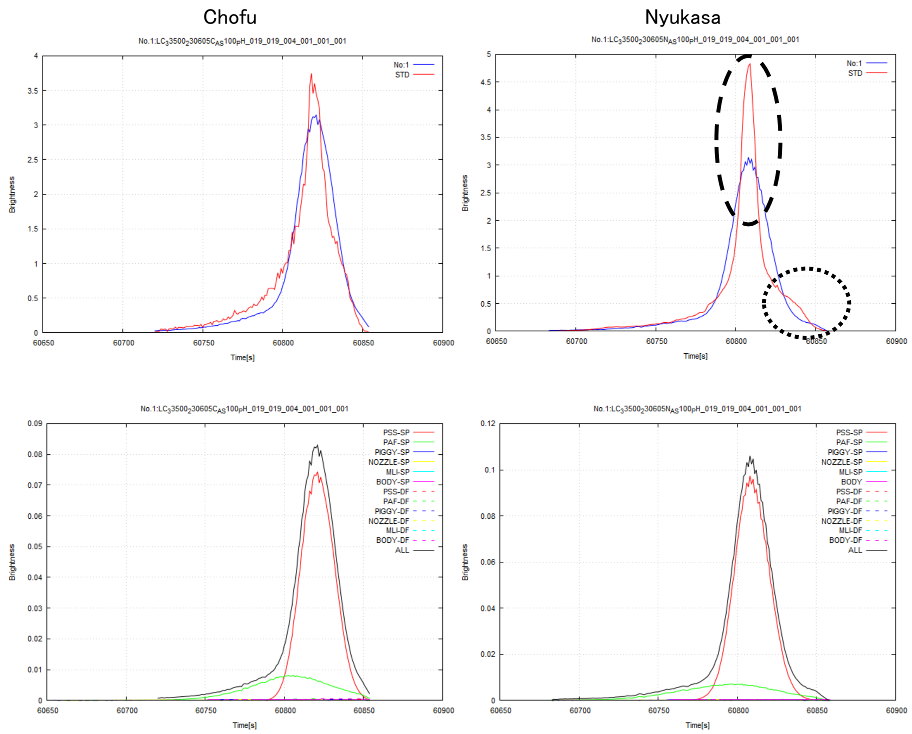

Figure 9. Top: The observed(blue) and simulated(red) light curves by the Chofu telescope(left) and the Nyukasa telescope(right) in the case of the lowest RSA value in the first step ($[R_1, R_2, R_3] = [180°, 0°, 30°]$). Bottom: Each reflection component of the simulated light curves.

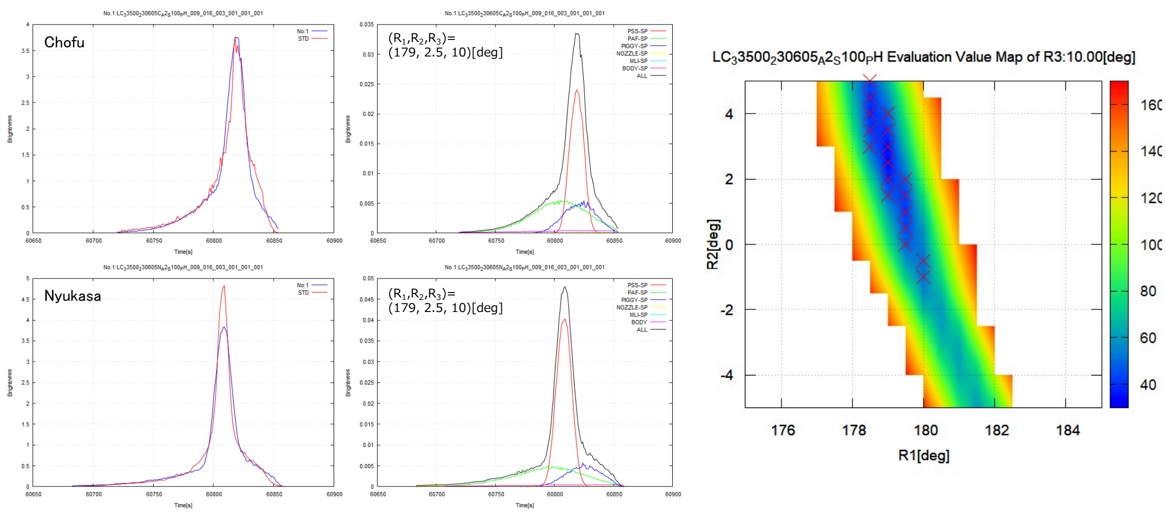

Figure 10. Left: Light curves in the case of the lowest RSA value in the second step ($[R_1, R_2, R_3] = [179.0°, 2.5°, 10.0°]$). Note that the diffuse reflection components are negligible therefore omitted for clarity in the figure. Right: RSA value map on $R_1 - R_2$ plane of $R_3 = 10.0°$ in the second step. The white region represent RSA values exceeding the maximum value of the color bar.

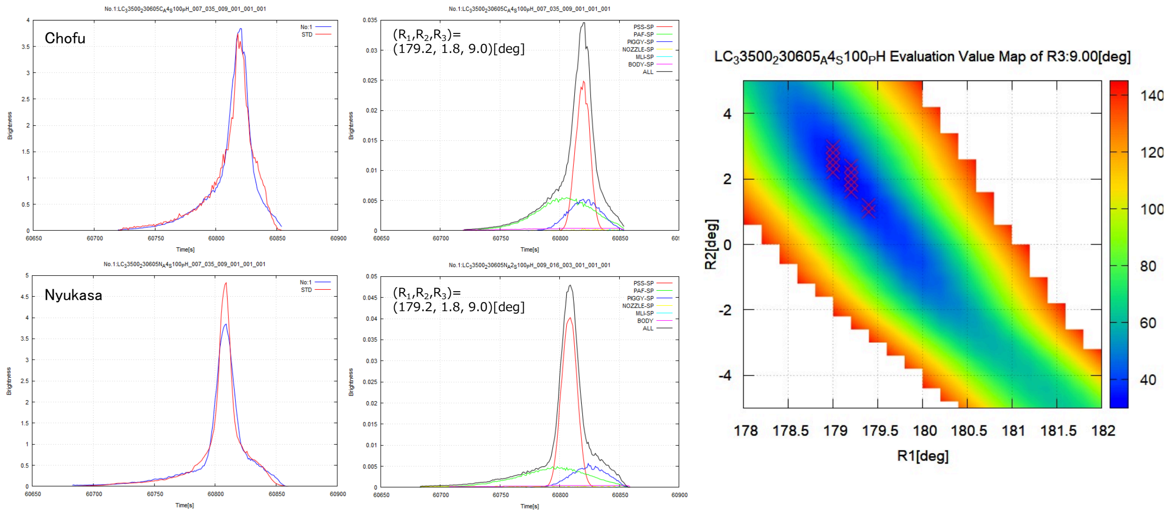

Figure 11. Left: Light curves in the case of the lowest RSA value in the fourth step ($[R_1, R_2, R_3] = [179.2°, 1.8°, 9.0°]$). Note that the diffuse reflection components are negligible therefore omitted for clarity in the figure. Right: RSA value map on $R_1 - R_2$ plane of $R_3 = 9.0°$ in the fourth step.

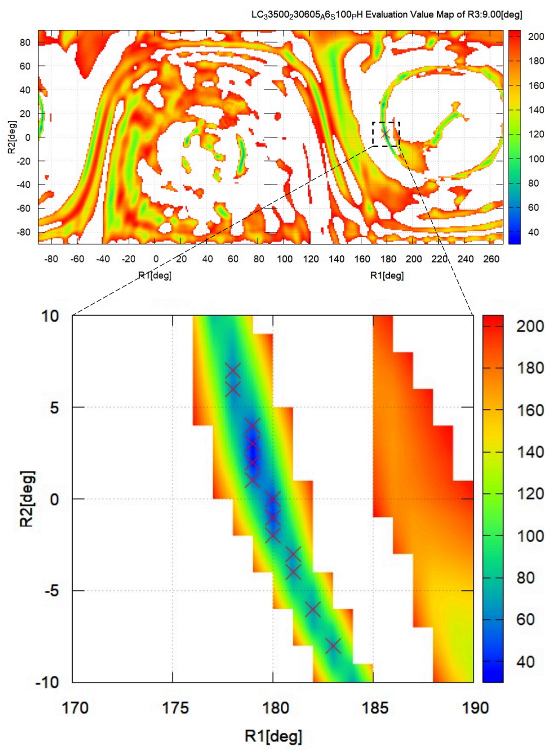

Figure 12. RSA value map on $R_1 - R_2$ plane of $R_3 = 9.0°$ with increments of $[\Delta R_1, \Delta R_2] = [1°, 1°]$ in the range of $[-90° < R_1 < 270°, -90° < R_2 < 90°]$

Table 4. Top 5 RSA values in the fourth step (in increments of $[R_1, R_2, R_3] = [0.2°, 0.2°, 0.5°]$ within the range $[178° < R_1 < 182°, -5° < R_2 < 5°, 5° < R_3 < 10°]$).

Rank	Total	Chofu	Nyukasa	R_1	R_2	R_3
1	32.134	14.869	17.265	179.2	1.8	9.0
2	32.369	15.658	16.711	179.0	2.6	9.5
3	32.377	15.436	16.941	179.2	2.0	9.0
4	32.437	16.637	15.801	178.8	3.4	10.0
5	32.520	14.926	17.595	179.6	0.6	7.5

4.2. Example of light curves having a single prominent peak

We present examples of the analysis results of the light curves having a single prominent peak in this subsection. Fig. 13 shows the analysis results of the light curves acquired using the Chofu telescope on 2024.04.25, 2024.05.09, 2024.07.28, 2024.08.13 in increments of $[\Delta R_1, \Delta R_2, \Delta R_3] = [1°, 1°, 1°]$ within the range $[175° < R_1 < 185°, -5° < R_2 < 5°, 40° < R_3 < 50°]$. In all cases, the peak is dominated by the specular reflection component from PSS.

4.3. Example of light curves having two prominent peaks

Fig. 14 shows the analysis results of the light curves acquired using the Chofu telescope on 2024.10.09, 2024.10.30, 2024.11.21, 2024.11.27. in increments

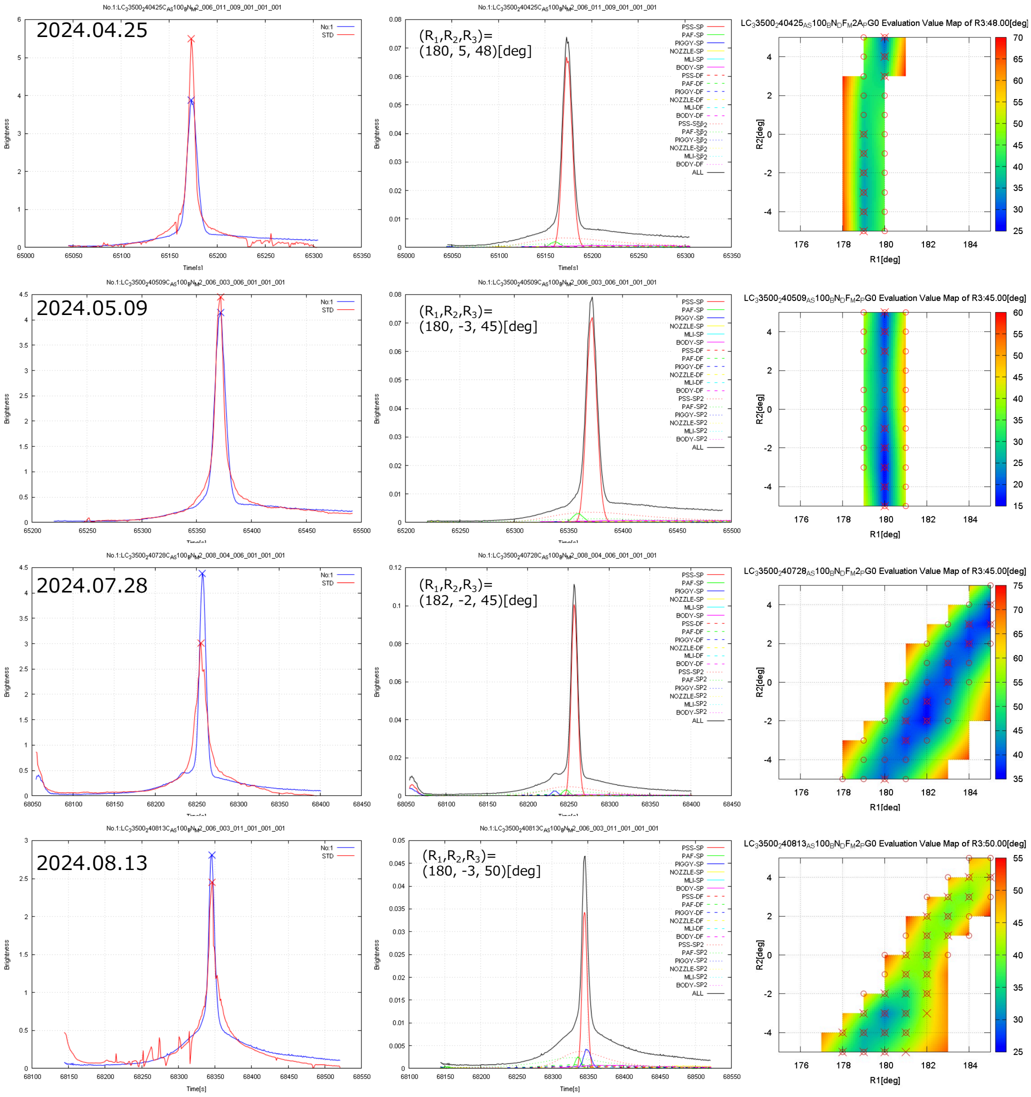

Figure 13. Observed(blue) and simulated(red) light curves(left), each reflection component of the simulated light curves(middle), and the RSA map(right) on 2024.04.25(top), 2024.05.09(second), 2024.07.28(third), 2024.08.13(bottom). All light curves are acquired using the Chofu telescope.

of $[\Delta R_1, \Delta R_2, \Delta R_3] = [1^\circ, 1^\circ, 5^\circ]$ within the range $[175^\circ < R_1 < 185^\circ, -5^\circ < R_2 < 5^\circ, 0^\circ < R_3 < 90^\circ]$.

These light curves show two prominent peaks dominated by the specular component from PSS. In such cases, the positions of both peaks are useful for narrowing down the solutions. In the evaluation map in Fig. 14, the red cross represents the case with the top 100 RSA values. In addition, the red circle represents the case where the position differences between the peaks in the observed and simulated light curves are less than 5 seconds. In these cases, the attitude estimations using the RSA values are consistent with those using the peak positions.

4.4. Example of light curves having a strong peak and a weak peak

Fig. 15 shows the analysis results of the light curves acquired using the Chofu telescope on 2024.10.01 and 2024.10.10 in increments of $[\Delta R_1, \Delta R_2, \Delta R_3] = [1^\circ, 1^\circ, 5^\circ]$ within the range $[175^\circ < R_1 < 185^\circ, -5^\circ < R_2 < 5^\circ, 0^\circ < R_3 < 90^\circ]$.

In the light curve on 2024.10.01, the weak peak is dominated by the extended specular reflection component (the second term of Eq.2) from PIGGY, while the strong peak is dominated by the specular reflection component from PSS. The attitude estimations using the RSA values are consistent with those using the peak positions.

On the other hand, in the light curve on 2024.10.10, the both peaks are dominated by the specular reflection component from PSS. A discrepancy in the position of the weak peak is observed between the observed and simulated light curves. In addition, there is a slight difference in the trend between the attitude estimation using the RSA values and the peak positions.

4.5. Example of light curves having no prominent peak

We also present the analysis result of the light curves having no prominent peak. Fig. 16 shows the analysis results of 13 light curve acquired using the Chofu telescope from 2023.05.15 to 2023.09.12 and the excluded areas map on the R_1-R_2 plane. The observed light curves are dim and have no prominent peaks. The simulated light curves are dominated by the diffuse reflection component. In such cases, the sensitivity of the RSA value to changes in attitude is low. Therefore, it is challenging to narrow down the candidate solutions for the attitude. Conversely, attitudes that result in sharp peaks are excluded from the candidate solutions.

5. DISCUSSION AND CONCLUSIONS

Light curves of the second stage of the Japanese H-2A rocket (H-2A R/B; International Designator 2009-002J/SSC 33500) were analysed to estimate its attitude. The light curve sometimes exhibits a prominent peak, which is dominated by the specular reflection component from PSS.

In cases where the light curves have no prominent peak, it is challenging to refine the candidate solutions for the attitude because the sensitivity of the RSA value to changes in attitude is low. However, even in such cases, we can exclude attitudes that result in prominent peaks from the candidate solutions.

In cases where the light curves have a single prominent peak, the candidate solutions are confined within a relatively narrow region on the RSA value map but still wide. When simultaneous light curves are acquired, the candidate solutions are confined to a narrower region.

In cases where the light curves have two prominent peaks, the candidate solutions are confined within a narrow region.

As a result of the comprehensive comparisons of observed and simulated light curves, we found that the light curves suggest that the attitude of target object is almost stationary, with the PAF pointing in the nadir direction, as expected from gravity-gradient stabilization. This is consistent with direct images obtained during the "Fly-around observation service" of the CRD2 mission.

Although the attitude during the period of each light curve is precisely estimated, particularly when the light curves have two prominent peaks, there is a slight variation in the estimated attitude between the light curves acquired during different observation periods (See Fig. 14). This result suggests the possibility of slight oscillations around the attitude expected from the gravity-gradient stabilization.

REFERENCES

1. Silha J, Pittet JN, Hamara M, Schildknecht T (2018). Apparent rotation properties of space debris extracted from photometric measurements. Advances in Space Research 61: 844-861.
2. Vananti A, Lu Y, Schildknecht T. (2023). Attitude Estimation of H2A Rocket Body from Light Curve Measurements. International Journal of Astrophysics and Space Science, 11(2), 15-22.
3. Yanagisawa T, Kurosaki H (2012). Shape and motion estimate of LEO debris using light curves. Advances in Space Research 50: 136-145.
4. Yanagisawa T, Hayashi M, Kurosaki H, Kawamoto S. (2021). Correlation Between Light Curve Observations and Laboratory Experiments Using a Debris Scale

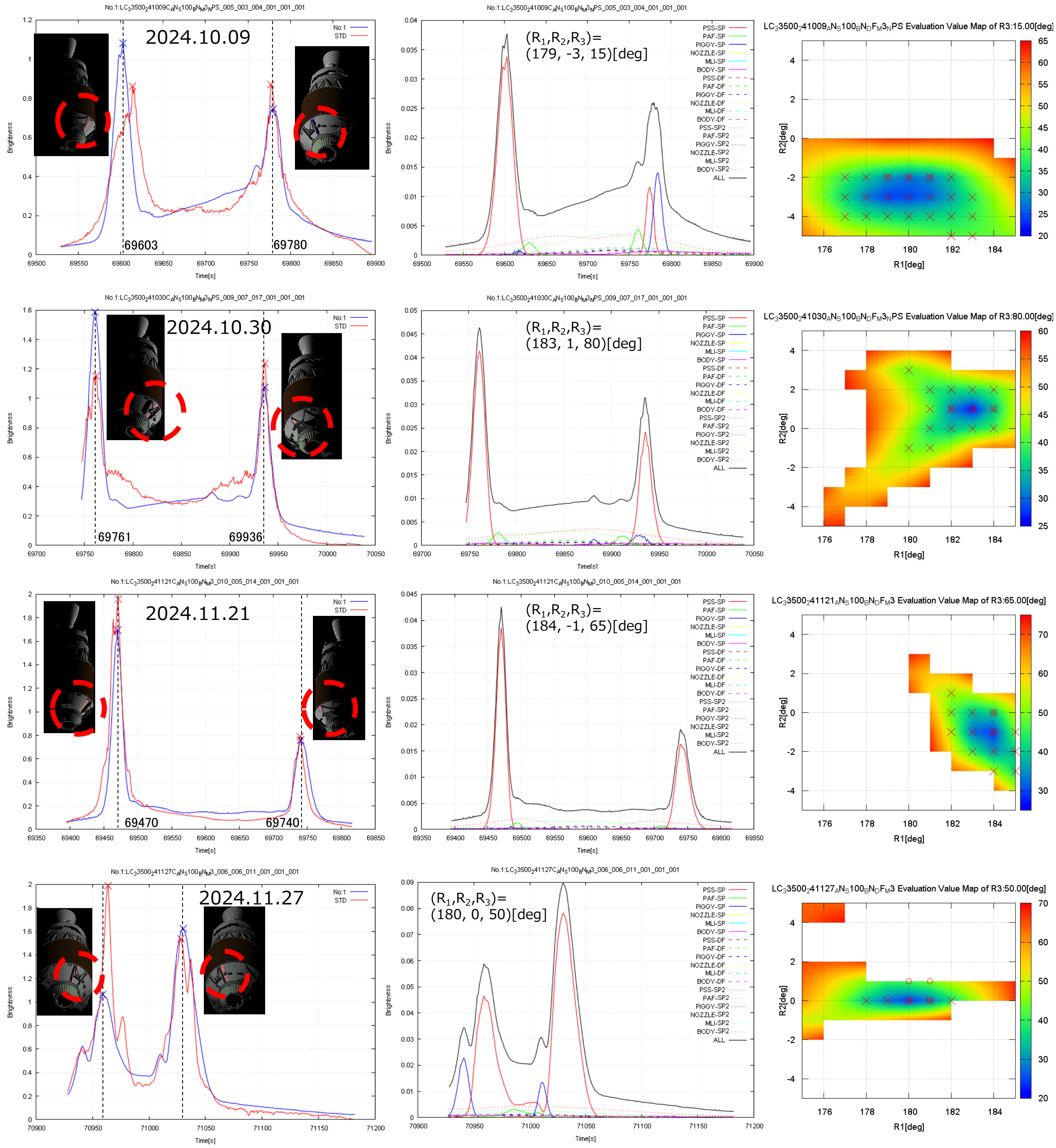

Figure 14. Observed(blue) and simulated(red) light curves(left), each reflection component of the simulated light curves(center), RSA value map on $R_1 - R_2$ plane(right) on 2024.10.09(top), 2024.10.30(second), 2024.11.21(third), 2024.11.27(bottom). All light curves are acquired using the Chofu telescope. The CG images at each peak are displayed. The dashed red circle represents the reflection area contributing each peak.

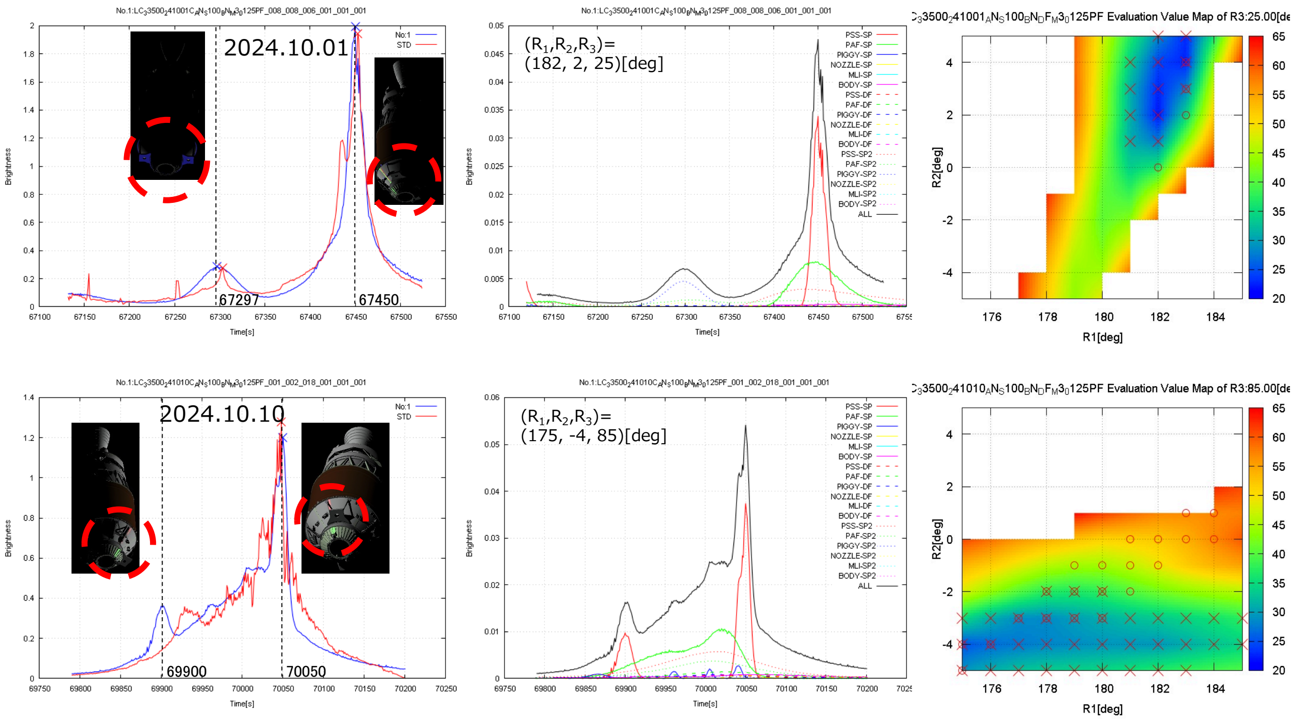

Figure 15. Observed(blue) and simulated(red) light curves(left), each reflection component of the simulated light curves(center), RSA value map on $R_1 - R_2$ plane(right) on 2024.10.01(top) and 2024.10.10(bottom). All light curves are acquired using the Chofu telescope.

Model in an Optical Simulator. Adv. Astronaut. Sci. Technol. 4, 47–54

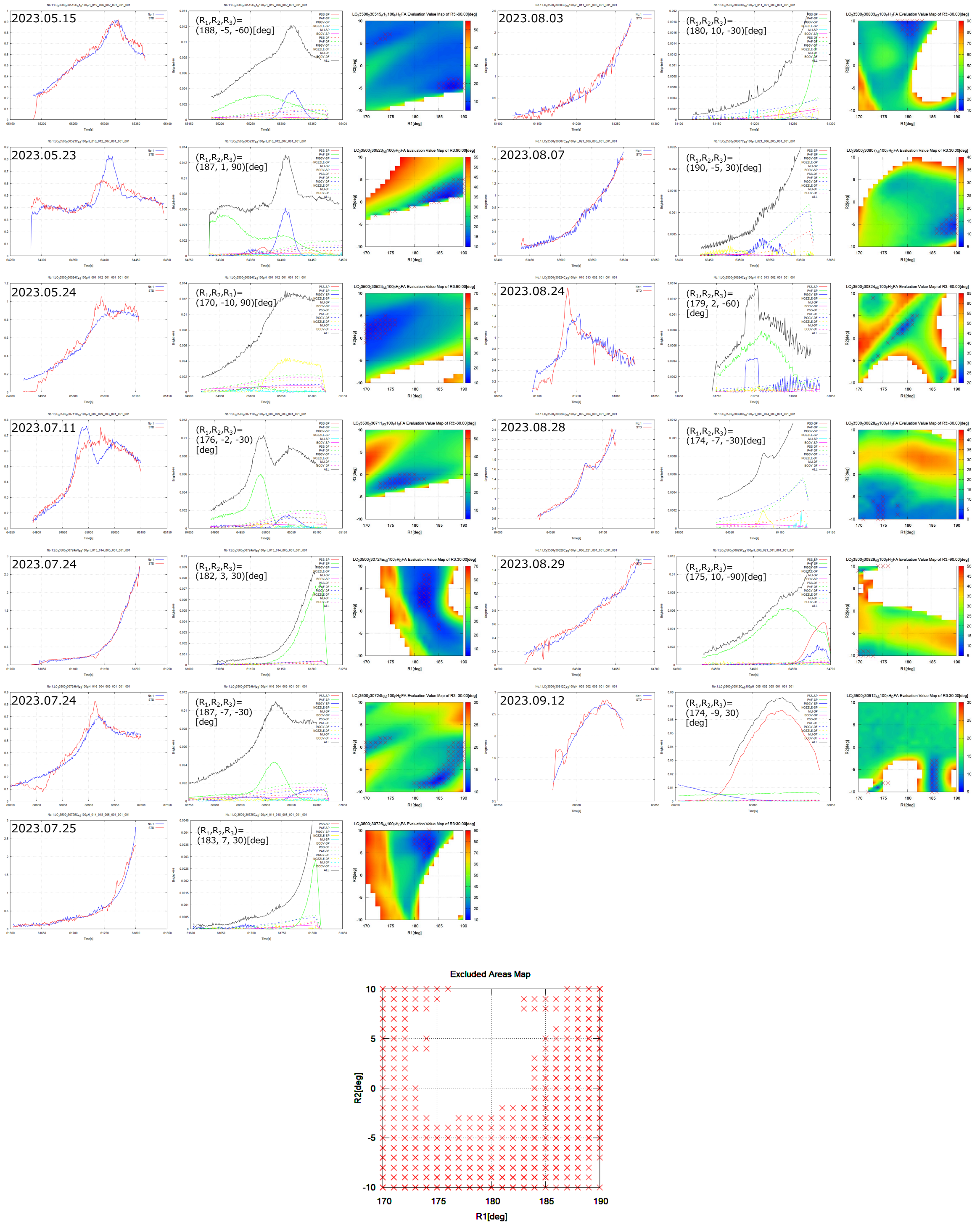

Figure 16. Top: Observed and simulated light curves, each reflection component of the simulated light curves, and RSA value map on the R_1-R_2 plane from 2023.05.15 to 2023.09.12 All light curves are acquired using the Chofu telescope. Bottom: Excluded areas map on the R_1-R_2 plane. Red cross represents the excluded solutions.